Research Article

Role of Surfaces in the Magnetic and Ozone Gas-Sensing Properties of ZnFe₂O₄ Nanoparticles: Theoretical and Experimental Insights

Regiane Cristina de Oliveira,* Renan Augusto Pontes Ribeiro, Guilherme Henrique Cruvinel, Rafael Aparecido Ciola Amoresi, Maria Helena Carvalho, Adilson Jesus Aparecido de Oliveira, Marisa Carvalho de Oliveira, Sergio Ricardo de Lazaro, Luís Fernando da Silva, Ariadne Cristina Catto, Alexandre Zirpoli Simões, Julio Ricardo Sambrano,* and Elson Longo

Read Online

ACCESS | Metrics & More | Article Recommendations | SI Supporting Information

ABSTRACT: The magnetic properties and ozone (O_3) gas-sensing activity of zinc ferrite ($ZnFe_2O_4$) nanoparticles (NPs) were discussed by the combination of the results acquired by experimental procedures and density functional theory simulations. The $ZnFe_2O_4$ NPs were synthesized via the microwave-assisted hydrothermal method by varying the reaction time in order to obtain $ZnFe_2O_4$ NPs with different exposed surfaces and evaluate the influence on its properties. Regardless of the reaction time employed in the synthesis, the zero-field-cooled and field-cooled magnetization measurements showed superparamagnetic $ZnFe_2O_4$ NPs with an average blocking temperature of 12 K. The (100), (110), (111), and (311) surfaces were computationally modeled, displaying the different undercoordinated surfaces. The good sensing activity of $ZnFe_2O_4$ NPs was discussed in relation to the presence of the (110) surface, which exhibited low (-0.69 eV) adsorption enthalpy, promoting reversibility and preventing the saturation of the sensor surface. Finally, the O_3 gas-sensing mechanism could be explained based on the conduction changes of the $ZnFe_2O_4$ surface and the increase in the height of the electron-depletion layer upon exposure toward the target gas. The results obtained allowed us to propose a mechanism for understanding the relationship between the morphological changes and the magnetic and O_3 gas-sensing properties of $ZnFe_2O_4$ NPs.

KEYWORDS: *ZnFe₂O₄, nanoparticles, O₃, sensor, magnetism, microwave hydrothermal*
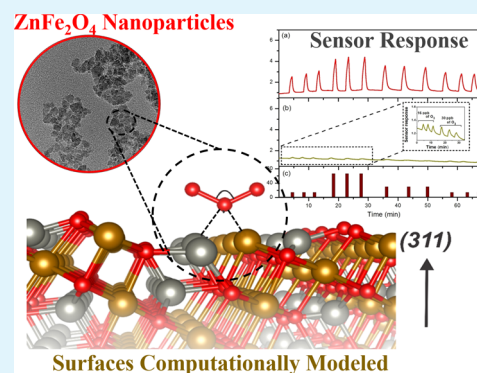
1. INTRODUCTION

The zinc ferrite ($ZnFe_2O_4$) nanoparticle (NP) is a metal–oxide semiconductor that has attracted much attention due to its high magnetic permeability, non-toxicity, narrow optical band gap (~1.92 eV), phase stability, and high electronic conductivity.[1−3] As a functional material, this is widely used for novel applications, such as hyperthermia cancer treatment, contrast agents, and gas sensors.[4−7]

Several studies report the efficiency of ferrites with magnetic properties in detecting gases, such as $CoFe_2O_4$,[8,9] $NiFe_2O_4$,[10] $MnFe_2O_4$,[11] and $ZnFe_2O_4$.[4,5,12−15] Magnetic sensors are a good alternative for the detection and measurement of different phenomena because they are a "simple" and readily available technology, they are resistant materials, favoring the construction of solid and reliable devices, and they can be developed without electric contact between the measuring device and the sensor, making them especially fit for use in harsh environments.[16] In special, $ZnFe_2O_4$ has been found to have sensing activity toward a wide range of organic gases, including acetone, ethanol, methanol, formaldehyde, and petrol, as well as inorganic gases, such as hydrogen sulfide

and nitrogen dioxide.[4,5,12−14] However, the ozone (O_3) gas-sensing property of $ZnFe_2O_4$ NPs has not been reported so far. It is important to mention that O_3 concentrations at the ppb level can cause lung diseases, respiratory diseases, and even death[17] Such facts explain the need to detect and continuously monitor O_3 levels, justifying the exploration of $ZnFe_2O_4$ NPs as O_3 gas sensors.

Control of morphology, and consequently the material surface, has a great influence on the physicochemical properties of the materials and serves as a powerful way to modulate the functional properties.[18−23] To the best of our knowledge, there has been no comprehensive experimental work, supported by theoretical simulations, specifically dealing with surface-dependent sensor and magnetic properties of $ZnFe_2O_4$

materials. Inspired by these reports, we aim to bridge the knowledge gap between theoretical and experimental results by preparing $ZnFe_2O_4$ NPs with different exposed surfaces. This integration not only points to a striking surface-dependent activity but also demonstrates how the understanding of the surface, at the atomic level, could pave the way for developing and/or enhancing optical and magnetic properties and sensing activity.

Numerous synthetic routes have been used for the preparation of $ZnFe_2O_4$ NPs, including sol−gel,[24] solvothermal,[25] and microwave-assisted hydrothermal (MAH) syntheses.[26] Compared to the other techniques, the MAH route is considered to be relatively simple, energetically efficient, environmentally friendly, and allows the control of particle morphology by variations in the synthesis parameters, such as pH, temperature, and so forth.[27]

In this study, $ZnFe_2O_4$ NPs were synthesized using the MAH route, and the reaction time was systematically varied in order to verify the influence of this parameter on the structural order (at long and short ranges), on the morphology, and consequently on the magnetic and sensing properties of the $ZnFe_2O_4$ NPs. To complement, density functional theory simulations were combined with experimental studies. For the first time in the literature, the surface of different morphologies was modeled in an attempt to establish an in-depth atomic level correlation between the structural, electronic, magnetic, and O_3 gas-sensing properties of $ZnFe_2O_4$ NPs, contributing to the understanding of the shape-oriented property control.

2. EXPERIMENTAL PROCEDURE

2.1. Synthesis and Characterization. To synthesize $ZnFe_2O_4$ NPs, 5 mmol of zinc nitrate hexahydrate ($Zn(NO_3)_2 \cdot 6H_2O$) (≥99.9%, Sigma-Aldrich) was first dissolved in 30 mL of distilled water under magnetic stirring at room temperature. Separately, 10 mmol of ferric nitrate nonahydrate $Fe(NO_3)_3 \cdot 9H_2O$ (99.0, Synth) was also dissolved in 30 mL of distilled water under the same conditions. After the complete dissolution of the reactants, the solutions were mixed at room temperature, and the pH of the resulting solution was adjusted to 13 with the addition of 6 mol L^{-1} of NaOH aqueous solution. Afterward, the solution was stirred for 10 min and then transferred to the MAH system at 160 °C and maintained there for different synthesis times: 2, 4, 8, 16, 32, and 64 min, which were used to name the samples along the text and figures (2, 4, 8, 16, 32, and 64 min). The materials were collected at room temperature, washed with distilled water until the pH was neutralized, and dried in a conventional furnace at 60 °C for 12 h.

All $ZnFe_2O_4$ samples were characterized by X-ray diffraction (XRD) using a Rigaku-DMax/2500PC (Japan) diffractometer, with Cu Kα radiation ($\lambda = 1.5406$ Å) in the 2θ range from 15° to 80° at a step size of 0.02° min^{-1}. Rietveld refinements were made using the General Structure Analysis System II (GSAS-II) in the 2θ range from 10 to 110° at a step size of 0.01° min^{-1}.[28] Raman scattering spectroscopy measurements were carried out using a T64000 spectrometer (HORIBA Jobin-Yvon, Japan) coupled to a CCD Synapse detector and an argon-ion laser operating at 633 nm with a maximum power of 7 mW. The spectra were measured in the range between 25 and 1200 cm^{-1}. Ultraviolet−visible diffuse reflectance spectroscopy (UV−vis) spectra were obtained using a Varian spectrophotometer (model Cary 5G, USA).

In order to verify the influence of the synthesis time on the morphological, sensing, and magnetic properties of $ZnFe_2O_4$ NPs, the techniques listed below were performed on the samples obtained at 2 and 64 min. The morphologies of the samples were examined by transmission electron microscopy (TEM) measurements using a FEI microscope (model Tecnai G2 F20, USA). Photoluminescence (PL) measurements were made with a Monospec 27 monochromator

(Thermal Jarrel Ash, USA) coupled to a R955 photomultiplier (Hamamatsu Photonics, Japan). A krypton ion laser (Coherent Innova 200 K, USA; $\lambda = 350$ nm) was used as the excitation source with an incident power of approximately 14 mW. All measurements were carried out at room temperature. X-ray photoelectron spectroscopy (XPS) measurements were conducted using a Scienta Omicron ESCA+ spectrometer system equipped with a hemispherical analyzer (EA125) and a monochromatic source of Al Kα (hν = 1486.7 eV). The C 1s peak at the binding energy of 285 eV was used in the analyses as the energy reference. Magnetization measurements as a function of the applied magnetic field (M vs H) and temperature (M vs T) were performed using a SQUID-VSM magnetometer (MPMS3-Quantum Design). The M vs T measurements with $H = 100$ Oe were made with zero-field-cooled (ZFC) and field-cooled (FC) protocols. The magnetic hysteresis curve was measured up to 70 kOe at 300 and 5 K. The $ZnFe_2O_4$ samples were measured in squid using gelatin capsules.

2.2. Computational Details. In order to corroborate the experimental results for $ZnFe_2O_4$, quantum-mechanical calculations in the density functional theory (DFT) framework were carried out using WC1LYP exchange−correlation functional implemented in CRYSTAL17 code.[29] The Zn, Fe, and O atoms were described by an atom-centered all electron basis set defined as 86-411d31G, 86-411d41G, and 8-411d1, respectively.[30] The crystalline structure was fully relaxed (in terms of atomic positions and cell lattice parameters) as a function of the total energy, and the electronic integration over the Brillouin zone was performed using a $6 \times 6 \times 6$ Monkhorst−Pack k-mesh.[31] Five thresholds were chosen to control the accuracy of the Coulomb and exchange integral calculations (8, 8, 8, 8, and 14). The root mean square (rms) gradient, rms displacement, maximum gradient, and maximum displacement were set to 3×10^{-4}, 1.2×10^{-3}, 4.5×10^{-4}, and 1.8×10^{-3} a.u., respectively.

Regarding the magnetic ordering, two collinear magnetic configurations, defined as ferromagnetic (FEM) and antiferromagnetic (AFM), were considered for the conventional (56-atom) unit cell, in agreement with other theoretical studies published in the literature.[32,33] The magnetic ground state was defined as the considered energy difference, that is, $\Delta E = E_{AFM} - E_{FEM}$. In this case, the most stable configuration was used for the electronic structural analysis.

Aiming at evaluating the role of $ZnFe_2O_4$ surfaces in the crystal morphology and gas-sensing properties, the (100), (110), (111), and (311) surfaces were modeled based on symmetric and nonstoichiometric slabs previously reported by Guo et al.[34] Here, the stability of each surface termination of zinc ferrite was investigated using a thermodynamic approach, as presented in the Supporting Information.

Regarding the magnetic properties of the $ZnFe_2O_4$ surface, the magnetization index (M) from the calculated spin density (D_μ) index of a given surface was calculated following the procedure previously reported by our group[35−38]

$$D_\mu = \frac{\mu_B}{A} \tag{1}$$

$$M = \sum c_{(hkl)} \cdot D_\mu^{(hkl)} \tag{2}$$

In short, this procedure consists of computing D_μ as the magnetic moment (μ_B) exposed along the (100), (110), (111), and (311) surface areas (A) and considering the surface composition for each morphology $c_{(hkl)}$, resulting in an overall magnetization index (M).

To further investigate the role of $ZnFe_2O_4$ surfaces in the O_3 gas-sensing properties of the NPs, adsorption models were constructed from (2×1) supercell expansions of previously optimized slabs. The adsorption enthalpy was calculated considering the basis set superposition error.

2.3. Sensor Preparation and Gas-Sensing Measurements. To perform gas-sensing measurements, the $ZnFe_2O_4$ NPs samples treated in the MAH system for 2 and 64 min were dispersed in isopropyl alcohol by an ultrasonic cleaner for 30 min. The obtained
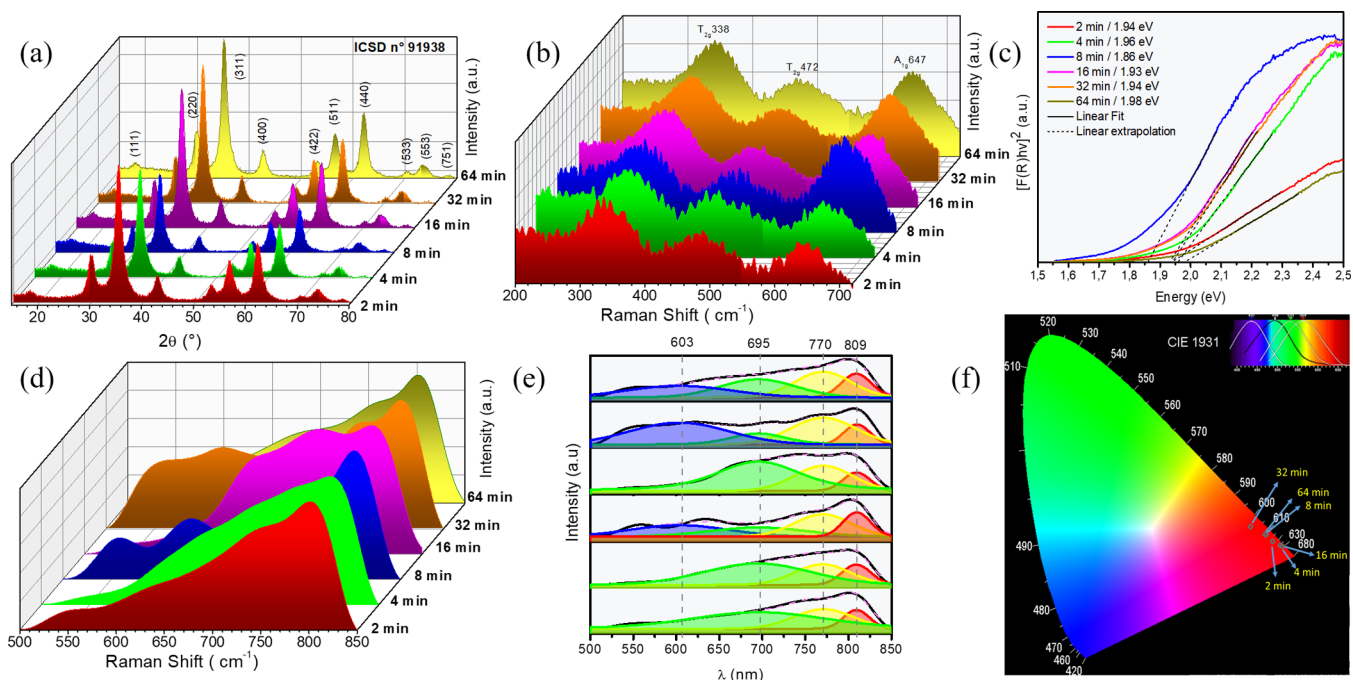
Figure 1. XRD patterns (a), Raman spectra (b), UV−vis diffuse reflectance (c), PL spectra (d), deconvolution of PL spectra (e), and (f) CIE chromaticity of $ZnFe_2O_4$ powders obtained by the MAH method at 160 °C by varying the time of synthesis.
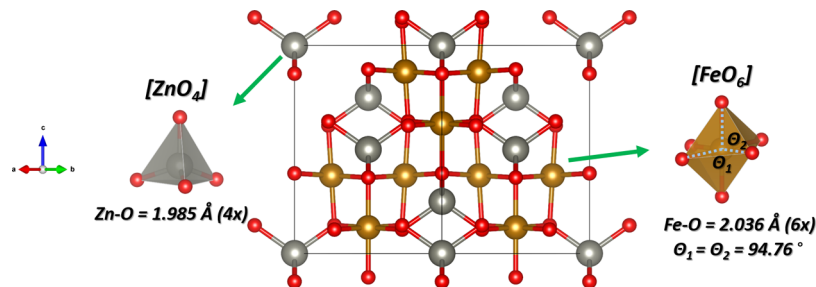
Figure 2. Schematic representation of optimized crystalline structure for $ZnFe_2O_4$ in the normal spinel structure. The gray, brown, and red balls represent the Zn, Fe, and O atoms, respectively, while the gray and brown polyhedrals refer to the $[ZnO_4]$ and $[FeO_6]$ clusters, respectively. The values in parenthesis correspond to the bond multiplicity.

suspensions were then dripped onto an Al_2O_3 substrate with interdigitated Pt electrode arrays with a thickness of 100 nm and spaced 50 μm apart. Afterward, the sensor samples were annealed for 30 min at 500 °C in an electric oven under an air atmosphere. The samples were inserted into a chamber, which allowed the control of the substrate temperature and O_3 levels. A 1 V dc voltage was applied to the sample, while the electrical resistance was monitored by means of a Keithley (model 6514) electrometer. Dry air was used both as a reference (baseline) and the carrier gas, maintaining a constant total flow equal to 500 sccm using mass flow controllers (Cole-Parmer US). The O_3 gas was generated using a pen-ray UV lamp (model P/N 90-0004-01), which oxidizes oxygen molecules from dry air, resulting in an O_3 output level from 14 to 66 ppb. The O_3 levels were calibrated by a toxic gas detector (ATI, model F12). The sensor response was defined as $S = R_{air}/R_{gas}$, where R_{air} and R_{gas} are the electric resistances of the device exposed to dry air and gas, respectively. Further details regarding the workbench used in the gas-sensing experiments can be found in the reference 39.

3. RESULTS AND DISCUSSION

3.1. $ZnFe_2O_4$ Crystal Order Analysis. A study of the influence of synthesis time on the order−disorder relationship between $ZnFe_2O_4$ NPs was carried out. To this end, the structural properties were characterized over long, short and

medium distances by XRD (Figure 1a), Raman (Figure 1b), UV−vis (Figure 1c), PL emission (Figure 1d,e), and CIE chromaticity (Figure 1f) techniques. To better understand and read the graphs presented in Figure 1, they are displayed separately and on a larger scale in the Supporting Information (see Figures S1a, S2−S6).

The XRD patterns of the $ZnFe_2O_4$ NPs obtained at different times using the MAH method show the synthesis of single-phase samples as all peaks can be indexed to the Inorganic Crystal Structure Database (ICSD) number 91938,[40] with face-centered cubic structure spatial group ($Fd\bar{3}m$) and eight molecular formulas per unit cell ($Z = 8$).

To better study the long-range properties of the $ZnFe_2O_4$ NPs, the Rietveld refinement technique was applied. The results are displayed in Figure S1b and Table S1 in the Supporting Information. The fitting parameters (wR %) indicate good agreement between the calculated and observed XRD patterns for all samples. We can note a nonlinear variation on the microstrain and wR %, which can be related to the crystallization−solubilization and recrystallization process promoted by microwave heating, capable of provoking the organization−disorganization and subsequent reorganization.
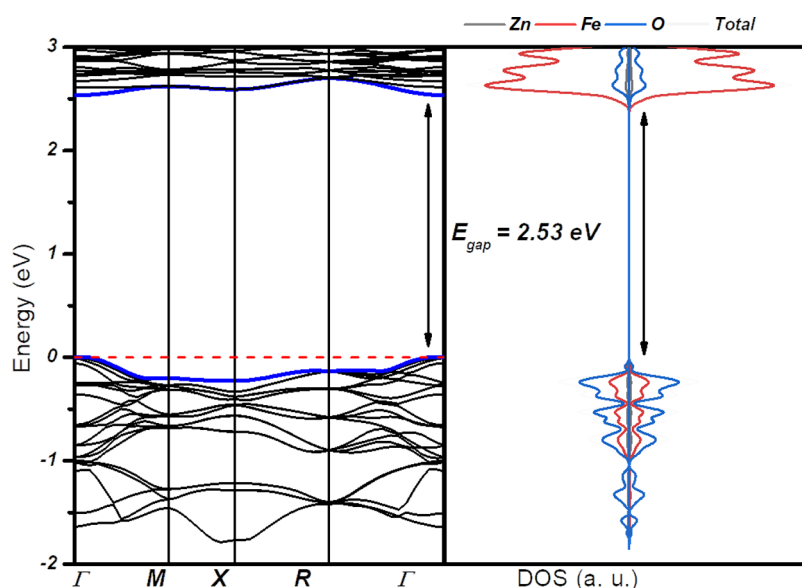
Figure 3. Band Structure and atom-resolved DOS for $ZnFe_2O_4$. In all cases, the Fermi levels were set to zero.

Since this phenomenon occurred randomly during the synthesis process, the NPs were formed with different structural defect densities, residual stresses, and distortions inside the lattice, independent of the synthesis time.[41] In addition, it is important to highlight that the experimental data obtained from Rietveld refinement showed that all samples have a normal spinel structure without cation inversion degree (x = 0.0).

The DFT optimized lattice parameters of $ZnFe_2O_4$ ($a = b = c$ = 8.471 Å) are in agreement with our experimental results obtained by Rietveld refinement (Table S1) and those published in the literature.[32,33,42] The optimized geometry is depicted in Figure 2, where we can see that the $ZnFe_2O_4$ NPs adopt a normal spinel structure with four- and six-fold Zn and Fe atoms, respectively, thus revealing the existence of $[ZnO_4]$ and $[FeO_6]$ clusters. In particular, the arrangement around Fe^{3+} atoms enables the division of the entire cubic structure in four sublattices containing $[FeO_6]_4$ connected by oxygen atoms, which are the essential blocks to understand the magnetic properties of $ZnFe_2O_4$ discussed in the upcoming sections.

A careful inspection of the obtained crystalline structure indicates that corner-sharing $[FeO_6]$ clusters are slighted distorted in relation to the Fe−O−Fe bond angle between the magnetic centers inside the individual sublattice. In the normal spinel of cubic symmetry, all B−O−B angles are expected to be orthogonal (90°). However, the obtained theoretical results revealed a bond angle of 94.76° for both in-plane and out-of-plane intermetallic connections. The angle in- and out-of-plane for Fe−O−Fe by the theoretical data and observed in the CIF file (experimental data) for all samples were presented in Table S1, in Supporting Information, where we can see a good correlation between the values. These results suggest that the electronic density in the crystalline structure has a singular distribution that favors different electronic transitions and magnetic behavior. These findings are in accordance with the (x, y, z) oxygen coordinates for all samples obtained by Rietveld refinement when compared to the literature.[32,33,42]

Consistent with the group theory analysis, the $ZnFe_2O_4$ has the following sets of optical phonon modes:[43] A_{1g} (R) + E_g (R)

+ T_{1g} (in) + 3 T_{2g} (R) + 2 A_{2u} (in) + 2 E_u (in) + 4 T_{1u} (IR) + 2 T_{2u} (in), where "R", "IR", and "in" represent Raman and infrared vibrations and inactive (silent) modes, respectively. Figure 1b shows the experimental Raman spectra of the as-synthetized $ZnFe_2O_4$ NPs, which are in agreement with those found in the literature.[32,33,42] The modes above 600 cm^{-1} are assigned to the $[ZnO_4]$ cluster, whereas those below this wavenumber are related to $[FeO_6]$ clusters.[44] According to Chandramohan et al.,[45] the A_{1g} mode is attributed to the symmetrical stretching in $[ZnO_4]$ clusters, while the other phonon modes below 600 cm^{-1} are due to symmetric and antisymmetric flexions of the oxygen−metal ions of Fe−O in the $[FeO_6]$ octahedron.

In the theoretical perspective, the five Raman active modes were predicted at 183.16, 363.28, 465.76, 595.85, and 689.63 cm^{-1} with T_{2g}, E_g, F_{2g}, F_{2g}, and A_{1g} symmetries, respectively. Following the experimental results, the observed T_{2g} mode at 472 cm^{-1} and A_{1g} mode at 647 cm^{-1} reasonably agree with the calculated values of 465.76 and 689.63 cm^{-1}, respectively. However, the experimental T_{2g} mode at 338 cm^{-1} does not agree with the theoretically predicted T_{2g} modes at 182.41 or 591.37 cm^{-1}, suggesting that the obtained samples show intrinsic structural disorder in the lattice, as evidenced by Rietveld refinement. Furthermore, it is important to point out that the additional differences between the obtained values can be related to the accuracy of some popular DFT methods for computing harmonic vibrational frequencies.[46]

All active Raman modes observed in Figure 1b are broad, suggesting that the $ZnFe_2O_4$ NPs synthetized at different times are structurally disordered at short range. Besides, the XRD and Rietveld refinement analyses indicated the presence of a symmetry break in the vibrational movements of the Zn, Fe and O atoms in the crystal lattice.

Figure 1c shows the UV−vis diffuse reflectance spectra of the $ZnFe_2O_4$ NPs. The Kubelka−Munk and Wood−Tauc functions were used to plot the $(F(R\infty)h\nu)^2$ versus $h\nu$ graph. The band gap energy (E_g) was determined by extrapolating the energy axis.[47,48] The results reveal that the $ZnFe_2O_4$ NPs synthesized at different times have an E_g of approximately 1.95 eV, which is in agreement with the literature.[43,49−51]
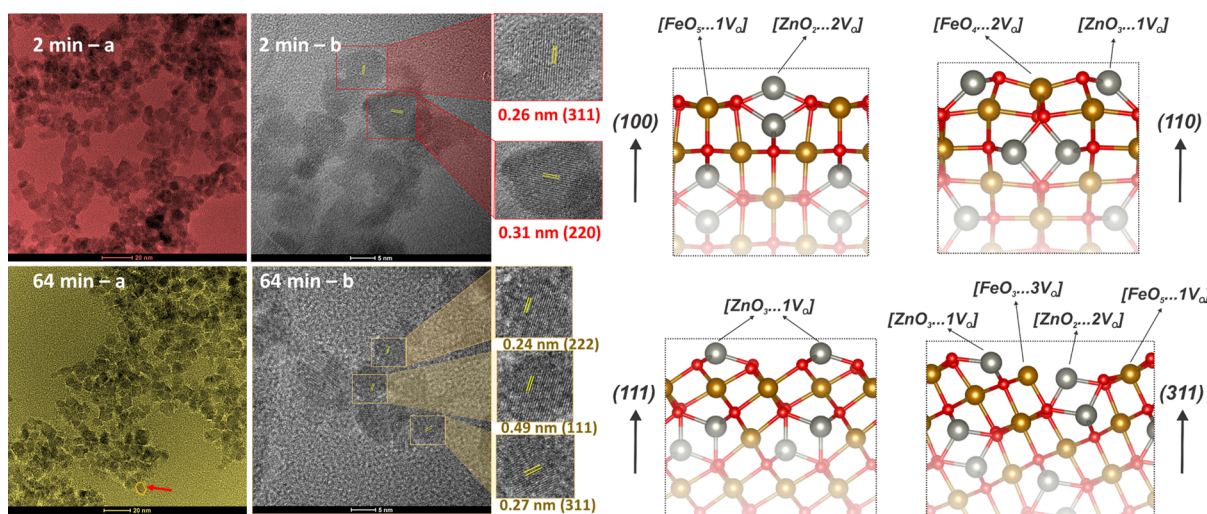
Figure 4. TEM and HRTEM images of $ZnFe_2O_4$ powders obtained by the MAH method at 160 °C for 2 and 64 min. In the right panel: representation of optimized (100), (110), (111) and (311) surfaces of $ZnFe_2O_4$ highlighting the chemical environment along the exposed plane.

The electronic transition observed from UV−vis spectroscopy can then be understood at the atomic level as an electron transfer mechanism involving filled 2p orbitals from O^{2-} anions and empty 3d states from Fe^{3+} cations. Indeed, the electron configuration for 3d^5 Fe^{3+} ($t_{2g}^3 e_g^2$) cation indicates the existence of half-filled 3d orbitals, which can receive only one electron, although the spin-forbidden rule of the electron transfer occurs due to the existence of opposite spins in the Fe^{3+} sublattices that originate the magnetic coupling. In the viewpoint of the theoretical evaluation, the electronic structure of $ZnFe_2O_4$ was investigated from the band structure and atom-resolved density of states (DOS) profiles, and the results are depicted in Figure 3. In this case, it can be observed that the valence band maximum is mainly composed of O 2p electronic states hybridized with Fe 3d orbitals, revealing a few extents of Zn, whereas the conduction band minimum is mostly composed of 3d empty states of Fe. The band structure indicates a direct (Γ−Γ) band gap around 2.53 eV and an additional indirect (Γ−X) transition around 2.59 eV. These values are not in accordance with our experimental results since the theoretical calculations were performed considering a perfect crystal, being the hybrid exchange−correlation treatment along with the existence of intrinsic defects in the samples the fundamental reasons behind the observed deviations.

However, a slope observed in the optical absorption curves (Figure 1c) of all samples is responsible for decreasing the E_g value. This slope is associated with the presence of defects in the NPs, which promote a reduction in E_g. For a perfect $ZnFe_2O_4$ crystal, we expected to observe a well-defined absorption curve and consequently an experimental E_g value of ∼2.5 eV (Figure 3) to reveal a good correlation with the theoretical value. Therefore, it can be stated that our $ZnFe_2O_4$ samples have electronic levels located within the prohibited band, which are associated with defects, such as distortions and vacancies, causing a structural lattice disorder previously observed in the XRD and Raman analyses.

In addition to the UV−vis analyses, PL analyses are also important to obtain electronic information on the structural organization degree (defects) in the material at medium range. These defects may be responsible for the appearance of intermediate levels between the VB and the CB, thus enabling

the PL emission at room temperature, according to Figure 1d. The $ZnFe_2O_4$ NPs showed broad PL emission bands, covering a large area of the electromagnetic spectrum. This is a typical profile of a multiphonic process, in which the emission occurs by several paths/states within the band gap of the material.[52] The delocalized electronic levels within the band gap were generated by intrinsic defect centers, as observed by XRD, Raman, and UV−vis analyses.

To understand the PL emission properties and their dependence on the structural order−disorder of the lattice, a deconvolution of the spectra was made using the Voigt area function in four pseudo-Voight: at 603 nm (blue), 695 nm (green), 770 nm (yellow), and 809 nm (red), as shown in Figure 1e. The percentage of area for each emission region is presented in Figure S6. It can be observed that the yellow and red emission regions remained practically constant in all samples. Nevertheless, the samples obtained at higher synthesis time presented emission in the blue region, besides a decrease in the green region. This behavior suggests that an increase in the synthesis time may lead to a greater variation in the shallow defects, such as distortions in the lengths and angles of the connections, since they are associated with the blue and green colors. In contrast, the deep defects related to the yellow and red colors, such as oxygen vacancies, still remained at different synthesis times.

Based on the PL spectra of the materials, the X- and Y-coordinates were calculated to estimate the emission color of the $ZnFe_2O_4$ NPs synthesized at different times by MAH. For this purpose, we used the Commission Internationale de l'Éclairage (CIE) chromaticity diagram, and the results are shown in Figure 1f. The emissions are centered in the red region, with a slight difference in color emission influenced by the synthesis time, indicating that $ZnFe_2O_4$ NPs are appropriate for applications in red lamps, displays, and other optical devices. Several biological benefits of red-light-based normal indoor lighting source are reported in the literature.[53]

3.2. Surface and Morphological Analyses. To better elucidate the morphology of the $ZnFe_2O_4$ NPs, Figure 4 shows TEM images of the samples. It is possible to observe that the synthesized NPs are agglomerated since very small particles tend to aggregate spontaneously to decrease their surface energy. Size measurements of the $ZnFe_2O_4$ NPs synthesized at
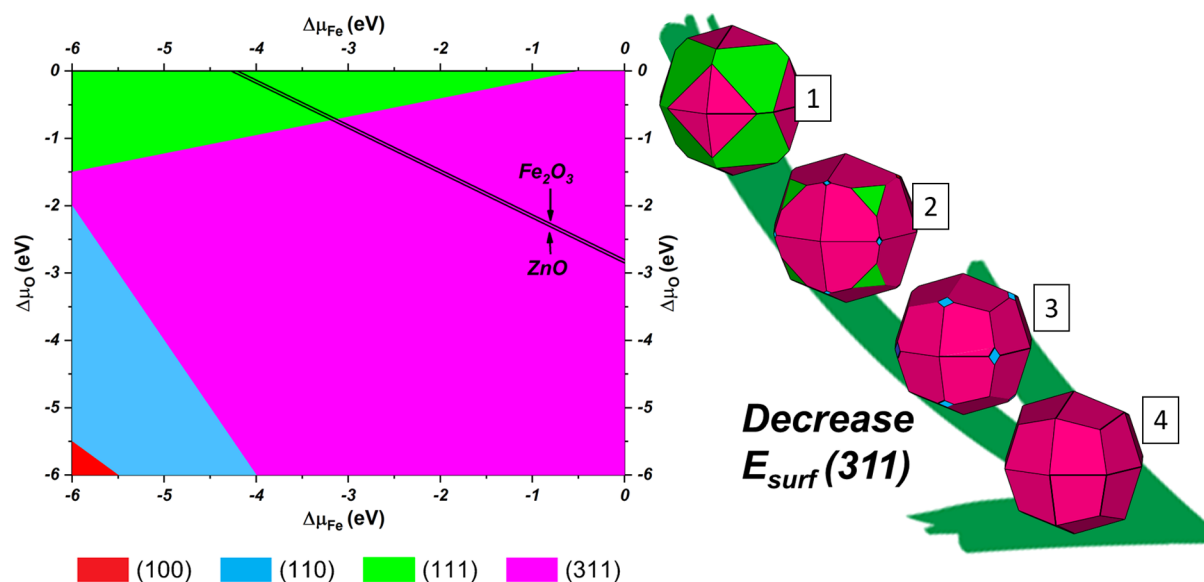
Figure 5. Phase diagram for $ZnFe_2O_4$ surfaces as functions of chemical potential for Fe and O atoms. The two lines inside the phase diagram indicate the region where $ZnFe_2O_4$ is stable in comparison to pure ZnO and Fe_2O_3 oxides. The numbers in the phase diagram specify the different conditions considered to obtain the morphologies depicted in the right panel.

2 and 64 min were performed, and the results are displayed in Figure S9. It can be seen that there were no significant changes in particle sizes for each sample, even with larger difference in the synthesis time. However, the sample synthesized at 64 min had a more definite contour, indicating that the reaction time significantly influences the morphology and crystallinity of $ZnFe_2O_4$ NPs, making it possible to create synthetic routes for the morphological control.

The high resolution TEM (HRTEM) images show that both samples (2 and 64 min) are crystalline, according to the well-defined lattice fringes observed. The spacing between neighboring slabs (lattice fringes) were measured and linked to the corresponding plane using the ICSD card number 91938.[40] For the $ZnFe_2O_4$ sample synthesized at 2 min, two different values were found: 0.26 and 0.31 nm, which correspond to the (311) and (220) surfaces. In contrast, for the sample synthesized at 64 min, it was possible to observe the (311), (222), and (111) planes with distances of 0.27, 0.24 and 0.49 nm, respectively. Furthermore, for comparative purposes, the distance between the (100), (110), (111), and (311) surface planes was obtained from DFT calculations, showing values of 0.42, 0.30, 0.49, and 0.25 nm, respectively, which are in agreement with experimental evaluations. It was also observed that different synthesis times results in the predominance of different surfaces in the samples. For instance, when the synthesis time increases, the (220) plane disappears, the (222) and (111) planes appear, and the (311) plane remains in the $ZnFe_2O_4$ NPs.

In the right side of Figure 4, it is possible to see the chemical environment of the (100), (110), (111), and (311) surfaces. We can note that the (311) surface exhibits a large degree of unsaturation, revealing different undercoordinated metal centers. On the other hand, the most regular exposed surface corresponds to the (111) plane, where tree-fold Zn cations are present. In addition, both (100) and (110) surfaces show a similar degree of undercoordination with five- and four-fold Fe centers, respectively, and two- and tree-fold Zn centers, respectively. Regarding the $ZnFe_2O_4$ properties, these distinct chemical environments can guide the existence of an intriguing

mechanism involving electronic, optical, and magnetic properties, as highlighted in the following sections.

The phase diagram for the (100), (110), (111) and (311) surfaces was analyzed. The Wulff construction[54] for the morphologies of $ZnFe_2O_4$ NPs as a function of Fe and O chemical potentials was applied, as depicted in Figure 5 and summarized in Table S2. Here, it is important to highlight that the γ values for such surfaces were calculated for slab models with a thickness of 12.08 (25 layers), 12.02 (17 layers), 13.38 (23 layers), and 11.54 Å (47 layers), respectively.

Taking into account the stability order of the investigated surfaces, it can be noted that the (311) surface exhibits an extensive stabilization range, followed by the (110), (111), and (100) surfaces (Figure 5 and Table S2). In particular, for the region, where $ZnFe_2O_4$ is stable (area enclosed by two lines in Figure 5), two main zones can be observed: (i) for oxygen-rich ($\Delta\mu_O = 0$ eV) and Fe-poor ($\Delta\mu_{Fe} = -4.25$ eV) domain, the (111) surface plane is the most stable and (ii) for oxygen-poor ($\Delta\mu_O = -2.75$ eV) and Fe-rich ($\Delta\mu_{Fe} = 0$ eV) environment, the (311) plane becomes the most stable exposed surface. These results infer a significant pattern for the obtained morphologies through the Wulff construction, as indicated in the right side of Figure 5.

A careful inspection of this map reveals a general rhombic shape for $ZnFe_2O_4$ surfaces enclosed by different extents of the (311), (111), and (110) surfaces. The first shape (1) shows a dominant character of the (111) surface (52.9%), with a minor extent of the (311) surface (47.1%). By reducing the chemical potential for O, the (111) surface gradually disappears, while the extent of the (110) and (311) planes increases. For the shape (2), the composition obtained was 0.5% for (110), 7.5% for (111), and 92.0% for (311). On the other hand, the shape (3) showed a composition of 2.0% for (110) and 98.0% for (311). Finally, in a Fe-rich environment, the rhombic shape (4) enclosed only by the (311) surface was obtained. By comparing the obtained results with the experimental TEM and HRTEM images, we could note an excellent agreement, indicating that the theoretically predicted morphological
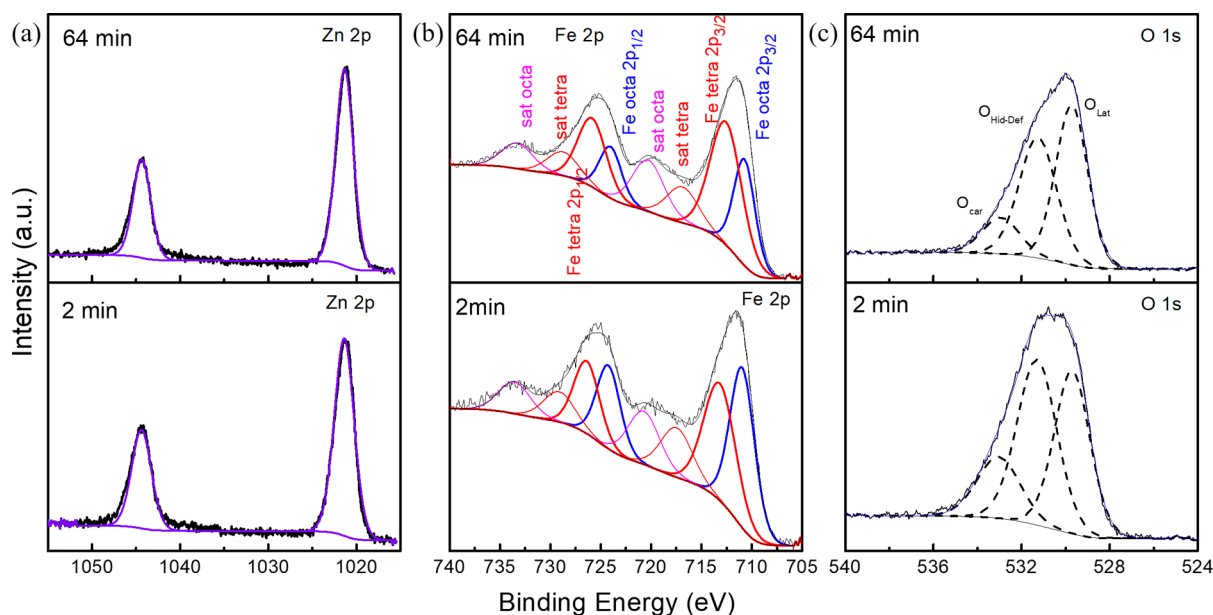
Figure 6. High resolution XPS for the Zn 2p, Fe 2p, and O 1s species for 2 min and 64 min $ZnFe_2O_4$ samples.

Table 1. XPS Analysis Results for O 1s of 2 and 64 min $ZnFe_2O_4$ Samples

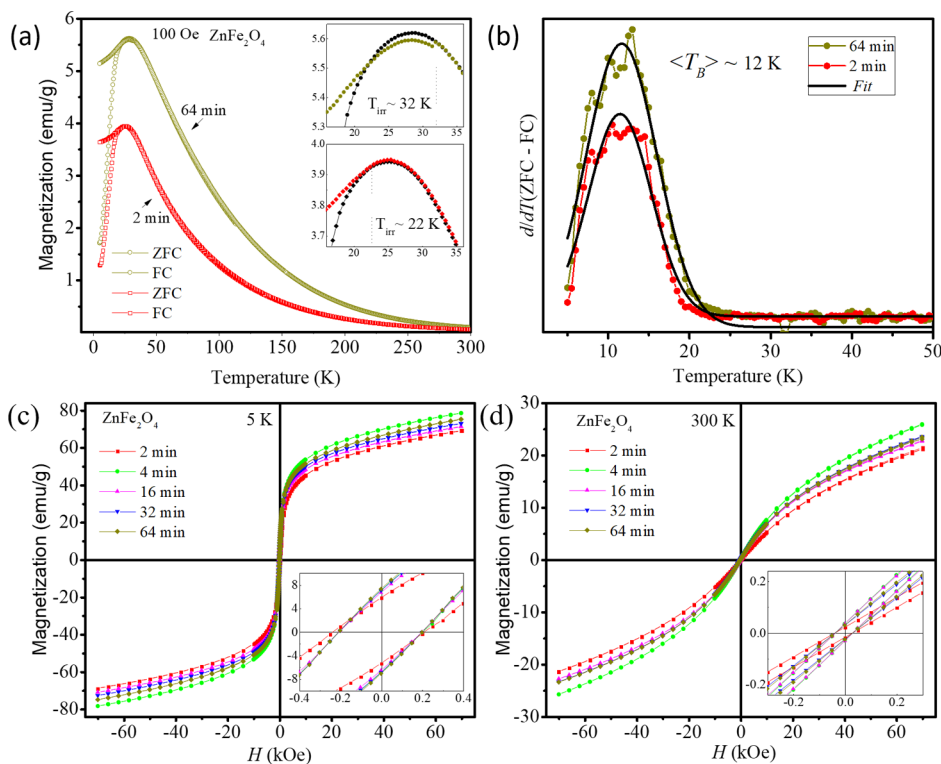|	O_{Lat}		$O_{Hid-Def}$		O_{car}	
	peak center (eV)	relative percentage (%)	peak center (eV)	relative percentage (%)	peak center (eV)	relative percentage (%)
2 min sample	529.7	38.6	531.2	43.7	532.9	17.7
64 min sample	529.7	46.7	531.3	41.0	533.0	12.3

Figure 7. (a) ZFC−FC magnetization curves measured at $H = 100$ Oe for $ZnFe_2O_4$ NPs synthesized for 2 and 64 min. The insets present an amplification of the curves, allowing the visualization of the estimated irreversibility temperature. (b) First derivative of the difference between ZFC and FC curves for the samples synthetized at 2 and 64 min, with the solid black lines representing the log−normal distributions. Magnetization curves as a function of the magnetic field measured at (c) 5 and (d) 300 K. The inset shows an amplification of the curves in the region of low magnetic field.

modulations obey the thermodynamic path observed in the experiments.

In order to further evaluate the composition of the surface of these materials, XPS analyses were performed. Figure 6a shows the Zn 2p spectrum with binding energy of 1021 and 1044 eV related to the $2p_{3/2}$ and $2p_{1/2}$ spin−orbit couplings, respectively, for both samples. This is due to the Zn(II) oxidation state and corresponds to the tetrahedral sites in $ZnFe_2O_4$. As shown in Figure 6b, the Fe 2p spectrum ranges from ~710 to 724 eV, relative to the octahedral site, and from ~713 to 726 eV, attributable to the tetrahedral site corresponding to the spin−orbit coupling of Fe $2p_{3/2}$ and Fe $2p_{1/2}$, respectively. The other peaks refer to the shakeup satellite structure. The above analyses are consistent with those previously reported in the literature[55−57] and indicate the Fe(III) oxidation state. It can be observed that between the two samples, the one with the shortest synthesis time has a higher proportion of peak area referring to the Fe ion octahedral site. This variation is closely related to the type of surface exposed in NPs since different surfaces present cluster types and coordinations with distinct anion and cation defects, as shown in the right panel of Figure 4.[58,59]

In particular, this fact can be associated with the increased extent of the (311) surface on the morphologies of the samples obtained with higher synthesis time. As displayed in Figure 4, the (110) and (311) surfaces contain the highest degree of undercoordination for Fe-centered clusters, exhibiting surface-exposed four-fold $[FeO_4]$ clusters in (110), while the (311) plane contains three-fold $[FeO_3]$ and five-fold $[FeO_5]$ clusters. Therefore, as the increase of synthesis time induces the disappearance of the (110) surface (left panel of Figure 4), the increased content of the (311) plane should be the major source of undercoordinated Fe centers observed in XPS analysis (Figure 6).

Figure 6c shows the O 1s spectrum fitted by three components: ~529, ~531, and ~533 eV. The peak in the lowest binding energy corresponds to lattice oxygen (O_{Lat}); the next one is linked to surface hydroxide and oxygen vacancies ($O_{Hid-Def}$); and finally the highest one is related to oxygen-bonded carbon species (O_{car}). It is observed that the 2 min sample has a 5% larger area related to oxygen vacancies than the 64 min sample, as seen in Table 1. We can then infer that the synthesis time influences cluster coordination, lattice mismatch, and oxygen defects, as observed according to the increase of the oxygen vacancy ratio.[56]

3.3. Magnetic Characterizations. Figure 7a shows the measurement of magnetization in the ZFC and FC protocols, performed at $H = 100$ Oe as a function of temperature ($5 \leq T \leq 300$ K) for the $ZnFe_2O_4$ samples synthesized at 2 and 64 min. The insets display an amplification of the ZFC−FC curves to allow the visualization of the estimated irreversibility temperature.

The ZFC−FC curves clearly reveal a typical behavior of a superparamagnetic system through the presence of a maximum associated with a blocking temperature, T_B, and a thermal hysteresis, evidenced by the deviation in the ZFC−FC curves at low temperatures. It is known that the derivative $d[(M_{ZFC} - M_{FC})/dT]$ is proportional to the blocking temperature distribution.[60,61] In this work, we used this calculation to estimate the mean blocking temperature $\langle T_B \rangle$, whose results, adjusted by a log−normal function, are shown in Figure 7b for 2 and 64 min samples. For both samples, we obtained the average blocking temperature of ~12 K as an adjustment

parameter of the log−normal function, which together with the TEM analyses, indicate the absence of significant variation in the average size of the NPs.[62] In addition, we observed a higher irreversibility temperature for the 64 min sample (see inset of Figure 7a), besides a broadening of the ZFC−FC curves. As also shown by the TEM images, such results suggest that the sample synthesized at 64 min has a distribution of mean particle size slightly larger than that obtained at 2 min.[63]

Figure 7c,d exhibits the M vs H curves measured at 5 and 300 K, respectively, with magnetic field ranging between −70 $\leq H \leq 70$ kOe for the samples synthesized at different times. For all samples, the M vs H curves also confirm the existence of a superparamagnetic system. For temperatures lower than the average blocking temperature (~12 K), the hysteresis curves at 5 K show coercive field, H_C, and remanence (see inset of Figure 7d), which are characteristic of the blocked regime. For temperatures higher than $\langle T_B \rangle$ (see inset of Figure 7d), the H_C and remanence values are negligible, characterizing the superparamagnetic regime. In addition, the H_C values are quite similar between the samples. For the sample with the shortest synthesis time (2 min), we estimated from the hysteresis curve a value of 215 Oe, which is slightly higher than that ($H_C = 203$ Oe) obtained for the 64 min sample.

Aiming at describing the magnetic structure of $ZnFe_2O_4$ NPs, it was possible to observe that the energy difference between the FEM and AFM indicates an AFM ground state with lower energy (14.68 meV/f.u.). Considering the ideal cubic symmetry for the normal spinel structure and the fact that Fe^{3+} has a $3d^5$ configuration, as previously discussed, a FEM interaction between magnetic $3d^5$ centers is expected for the orthogonal arrangement of the Fe−O−Fe superexchange coupling constant. However, the optimized crystalline structure depicted in Figure 2 has a local disorder along the $[FeO_6]$ clusters, which slightly distorts the Fe−O−Fe (94.76°) interaction inside the $[FeO_6]_4$ magnetic sublattice, resulting in a non-orthogonal interaction between the half-filled 3d orbitals from neighboring Fe^{3+} centers and a local AFM arrangement that spreads along the crystalline structure due to the dominant character associated with the third-neighbor interactions.

The magnetic properties are influenced by the morphology of the materials and the surface exposed planes. In especial, the surface can be controlled during the synthesis by the variation of the experimental conditions, such as surface modifications due to coating with acid or oxides,[64] use of an inorganic non-magnetic matrix to reduce the effect of magnetic interaction between the and the annealing process, for example.[65] To analyze the role of $ZnFe_2O_4$ morphologies in the magnetic properties, the magnetization index (M) was calculated for each morphology depicted in Figure 7, following eqs 1 and 2. According to AFM ground for the $ZnFe_2O_4$ bulk, the overall magnetic ordering of the (100), (110), (111), and (311) surfaces demonstrates that they exhibit a spin-compensated arrangement, except for the (311) plane. In other words, the exposed Fe centers along such planes are antiferromagnetically ordered. For the (311) surface, the intriguing chemical environment (Figure 4) induces a FEM arrangement for the exposed spins, leading to a magnetization density around 7.98 μ_B/nm^2. Therefore, it is expected that by controlling the exposure of the (311) surface, the overall magnetization will be tailored considering the existence of uncompensated spins along the exposed plane.

Indeed, by computing the overall M for each morphology (Figure 5), we could observe that the M value for shape (1)
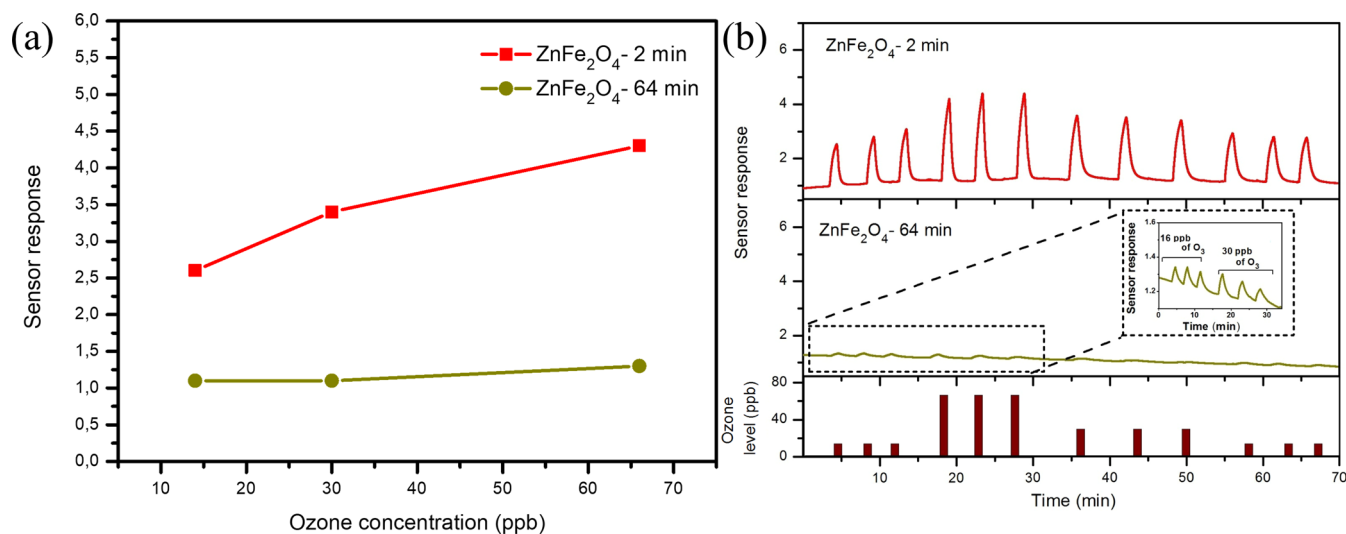
Figure 8. Ozone gas-sensing properties of $ZnFe_2O_4$ samples (a) exposed to 16 ppb of O_3 at different operating temperatures and (b) exposed to different O_3 levels (14, 30, and 66 ppb) at an operating temperature of 200 °C.
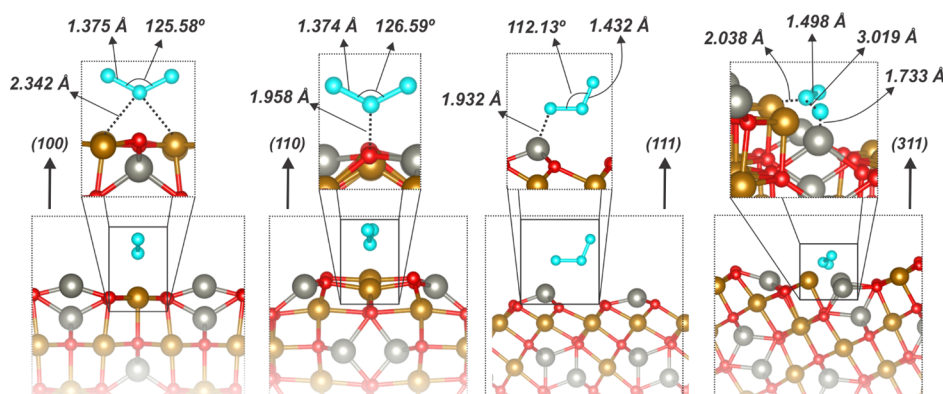
Figure 9. Optimized geometries for O_3 (cyan) adsorption along (100), (110), (111), and (311) $ZnFe_2O_4$ surfaces.

was 3.76. With the increase in the exposure of (311) through the control of its surface energy in the phase diagram, the magnetization increased to 7.34 (2), 7.82 (3), and 7.98 (4). Therefore, through the analysis of the magnetization curves reported in Figure 7, we can argue that the control of the MAH synthesis time induces the control of the exposure of (311), resulting in different magnetization values observed in the experiment.

3.4. Gas-Sensing Properties. Gas-sensing tests were performed by exposing the samples to 14 ppb of O_3 for 30 s at different temperatures (from 200 to 350 °C) in order to find the optimum operating temperature. Figure 8a illustrates the sensor response as a function of the operating temperature for $ZnFe_2O_4$ samples synthesized at 2 and 64 min in the MAH system. At relatively high temperatures (e.g., above 250 °C), the sensors exhibit very low response toward the different O_3 levels here evaluated (14, 30, and 66 ppb). It can be seen that as the operating temperature decreases, the responses increase, reaching a maximum value at around 200 °C. Both $ZnFe_2O_4$ NPs samples present electrical resistance at temperatures below 200 °C, leading to experimental limitations. Therefore, to evaluate the gas-sensing performance of the $ZnFe_2O_4$ NPs when exposed to different O_3 levels, the working temperature was then fixed at 200 °C, and the dynamic response–recovery characteristic toward various O_3 levels was investigated. The

dynamic cycles of the $ZnFe_2O_4$ NPs (2 and 64 min in the MAH system) are displayed in Figure 8b, considering an O_3 exposure between 14 and 66 ppb. Three exposure cycles of 60 s were collected at each concentration.

The sensor response for the $ZnFe_2O_4$ sample synthesized at 2 min was approximately 2.5, 3.7, and 4.2 for O_3 levels of 14, 30, and 66 ppb, respectively. It should be noted that these consecutive exposures did not poison the sample surface, and even after several exposure cycles, this sample could still detect low ozone concentrations (14 ppb), demonstrating good reversibility. As depicted in Figure 8b, the sample synthesized at 64 min also detected all O_3 gas concentrations investigated, yet with a very low response ($S = 1.3$), even for the highest O_3 gas level (66 ppb). Additionally, the response of this sample remained unchanged in relation to ozone gas concentration, indicating that its saturation level was reached.

The ozone gas-sensing mechanism can be explained based on the conduction changes of the $ZnFe_2O_4$ surface.[66] In ambient air, the oxygen molecules capture free electrons from $ZnFe_2O_4$ surfaces, thus forming oxygen anions ($O_{2(ads)} + 2e^- \rightarrow 2O_{(ads)}^-$).[67] Then, when the O_3 gas is introduced into the environment, the analyte interacts with the $ZnFe_2O_4$ compound, causing the O_3 molecules to react with the anions adsorbed onto the $ZnFe_2O_4$ surfaces, as represented in the following reactions[39]

$$O_{3(g)} + e^- \rightarrow O_{3(ads)}^- \tag{3}$$

$$O_{3(ads)}^- + O_{(ads)}^- + 2e^- \rightarrow O_{2(g)} + 2O_{2(ads)}^- \tag{4}$$
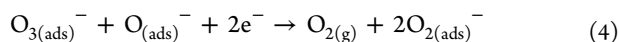
As a consequence of this reaction, the electrons are removed from the $ZnFe_2O_4$ conduction band, leading to an enhancement of the electron-depletion layer height, increasing the electrical resistance of the $ZnFe_2O_4$ compound upon exposure toward O_3 gas.[68]

In order to understand the role of $ZnFe_2O_4$ surfaces in the O_3 gas-sensing properties of the NPs, the adsorption models were calculated. Figure 9 summarizes the obtained geometries after O_3 adsorption along the (100), (110), (111), and (311) surfaces. For the (100) surface, the O_3 molecule is adsorbed bridging five-fold Fe centers with an adsorption enthalpy of −0.69 eV. To maintain the geometry of the O_3 molecule, this adsorption is classified as physical adsorption. Similar results were found for the (110) surface, being the major difference the value associated with the direct pointed adsorption at four-fold Fe centers, featuring an adsorption enthalpy around −0.64 eV. On the other hand, for the (111) plane, the adsorption of the O_3 molecule is pointed along tree-fold Zn centers, with an increased adsorption enthalpy of −1.76 eV. Here, it is important to highlight that the increased adsorption energy is associated with the drastic deformation of the O_3 geometry, suggesting a bond-breaking mechanism after adsorption. Therefore, this case can be considered as chemical adsorption since this process is responsible for activating the dissociation of O_3 along the exposed surface. Studies developed by Ren et al. also demonstrate that different surface arrangements generate electrostatic potentials that induce the effective adsorption of molecules.[69]

Finally, for the (311) surface, the obtained results indicate that the O_3 molecule is broken after adsorption, resulting in the formation of new Zn−O and Fe−O chemical bonds at two-fold Zn and tree-fold Fe centers. Consequently, the O_3 gas becomes O_2, which in turn is stabilized by neighboring tree-fold Fe centers that adsorb this species. These results justify the increased adsorption enthalpy calculated as −9.43 eV, which can be classified as dissociative because of the high degree of undercoordination of the pristine (311) surface. Therefore, the calculated adsorption enthalpy order is as follows: (110) < (100) < (111) < (311).

By combining the experimental and theoretical analyses for the $ZnFe_2O_4$ gas-sensing properties, we can make some assumptions. First, the best gas-sensing response of the $ZnFe_2O_4$ NPs obtained at 2 min can be associated with the existence of the (110) surface. The low adsorption enthalpy of this surface allows only physical adsorption. In this case, the active sites are easily recovered and made available again to keep the sensor activity, enabling reversibility, increasing high gas response, and preventing saturation of the sensor surface. Second, the observed sensor saturation of the $ZnFe_2O_4$ NPs obtained at 64 min can be associated with the (311) and (111) surfaces. The O_3 molecular adsorption on these surfaces provokes the poisoning of the active sites, reducing their subsequent adsorption and consequently creating a monolayer of oxygen atoms along the exposed surfaces. In addition, the results of XRD, Raman, UV−vis, and PL analyses show that the samples synthesized at shorter times are more disordered. The XPS measurements also reveal that NPs synthesized at 2 min have a higher number of oxygen vacancies, which contributes to their greater sensing activity. To corroborate

our discussion, it has been shown in the literature that the gas adsorption behavior is not directly correlated with the adsorption energy; instead, the adsorption energy is closely related to the sensitivity of gas-sensitive materials.[70]

4. CONCLUSIONS

For the first time, a complete study about the electronic, structural, optical, and magnetic properties as well as the morphological evolution of $ZnFe_2O_4$ NPs was conducted so as to correlate the gas sensor activity of this material by joining experimental methods and first-principle simulations. The surface of the $ZnFe_2O_4$ NPs was optimized by Wulff crystal construction, and a good arrangement between experimental and theoretical morphologies was establish.

The magnetic analyses indicated a characteristic super-paramagnetic regime for the NPs. The overall magnetic ordering simulations of surfaces demonstrated that the (311) plane exhibited a spin-compensated arrangement when compared to the other surfaces. The O_3 gas-sensing analyses showed that the 2 min sample could detect low O_3 concentrations and with good reversibility characteristics. The 64 min sample also detected all O_3 gas concentrations, yet with a much lower sensor response.

The theoretical and experimental results allowed us to conclude that the increased O_3 gas-sensing property of the $ZnFe_2O_4$ NPs obtained at 2 min can be associated with the presence of the (110) surface, which presented low reactivity toward O_3, enabling reversibility and higher gas response, and consequently preventing the saturation of the sensor surface. In conclusion, our research brings a new perspective on the influence of different surfaces of $ZnFe_2O_4$ NPs on the magnetic properties and O_3 gas adsorption mechanism, based on results from theoretical simulations, magnetization measurement, and gas-sensing experiments.

■ ASSOCIATED CONTENT

Ⓢ Supporting Information

The Supporting Information is available free of charge at https://pubs.acs.org/doi/10.1021/acsami.0c15681.

> Details of samples used for the characterization techniques and how were the samples prepared for TEM e gas-sensing measurements, graphs displayed separately and on a larger scale to improve the visualization and reading of the graphs, results obtained from Rietveld refinements and theoretical simulations, and size measurements of the $ZnFe_2O_4$ NPs synthesized at 2 and 64 min and the results (PDF)

■ AUTHOR INFORMATION

Corresponding Authors

Regiane Cristina de Oliveira − *Modeling and Molecular Simulations Group, São Paulo State University, UNESP, Bauru, São Paulo 17033-306, Brazil; Faculty of Engineering of Guaratinguetá, São Paulo State University, UNESP, Guaratinguetá, São Paulo 12516-410, Brazil;* ⓞ orcid.org/0000-0002-7332-8731; Email: g.ianeoliveira@hotmail.com

Julio Ricardo Sambrano − *Modeling and Molecular Simulations Group, São Paulo State University, UNESP, Bauru, São Paulo 17033-306, Brazil;* Email: jr.sambrano@unesp.br

Authors

Renan Augusto Pontes Ribeiro − *Department of Chemistry, State University of Minas Gerais, 35501-170 Divinópolis, Minas Gerais, Brazil; Functional Materials Development Center, Federal University of São Carlos, UFSCar, São Carlos, São Paulo 13565-905, Brazil;* ● orcid.org/0000-0002-4128-8296

Guilherme Henrique Cruvinel − *Functional Materials Development Center, Federal University of São Carlos, UFSCar, São Carlos, São Paulo 13565-905, Brazil*

Rafael Aparecido Ciola Amoresi − *Faculty of Engineering of Guaratinguetá, São Paulo State University, UNESP, Guaratinguetá, São Paulo 12516-410, Brazil;* ● orcid.org/0000-0002-7523-6013

Maria Helena Carvalho − *Physics Department, Federal University of São Carlos, (UFSCar), 13565-905 São Carlos, São Paulo, Brazil*

Adilson Jesus Aparecido de Oliveira − *Physics Department, Federal University of São Carlos, (UFSCar), 13565-905 São Carlos, São Paulo, Brazil*

Marisa Carvalho de Oliveira − *LSQM−Laboratory of Chemical Synthesis of Materials, Department of Materials Engineering, Federal University of Rio Grande do Norte, 59078-900 Natal, Rio Grande do Norte, Brazil;* ● orcid.org/0000-0003-3392-7489

Sergio Ricardo de Lazaro − *Department of Chemistry, State University of Ponta Grossa, 84030-900 Ponta Grossa, Paraná, Brazil;* ● orcid.org/0000-0001-9753-7936

Luís Fernando da Silva − *Laboratory of Nanostructured Multifunctional Materials, Federal University of São Carlos, 13565-090 São Carlos, São Paulo, Brazil;* ● orcid.org/0000-0001-6257-5537

Ariadne Cristina Catto − *Functional Materials Development Center, Federal University of São Carlos, UFSCar, São Carlos, São Paulo 13565-905, Brazil*

Alexandre Zirpoli Simões − *Faculty of Engineering of Guaratinguetá, São Paulo State University, UNESP, Guaratinguetá, São Paulo 12516-410, Brazil*

Elson Longo − *Functional Materials Development Center, Federal University of São Carlos, UFSCar, São Carlos, São Paulo 13565-905, Brazil;* ● orcid.org/0000-0001-8062-7791

Complete contact information is available at:
https://pubs.acs.org/10.1021/acsami.0c15681

Notes

The authors declare no competing financial interest.

■ REFERENCES

(1) Tatarchuk, T. R.; Paliychuk, N. D.; Bououdina, M.; Al-Najar, B.; Pacia, M.; Macyk, W.; Shyichuk, A. Effect of Cobalt Substitution on Structural, Elastic, Magnetic and Optical Properties of Zinc Ferrite Nanoparticles. *J. Alloys Compd.* **2018**, *731*, 1256−1266.

(2) Aisida, S. O.; Ahmad, I.; Ezema, F. I. Effect of Calcination on the Microstructural and Magnetic Properties of Pva, Pvp and Peg Assisted Zinc Ferrite Nanoparticles. *Physica B: Condensed Matter* **2020**, *579*, 411907.

(3) Jishkariani, D.; Lee, J. D.; Yun, H.; Paik, T.; Kikkawa, J. M.; Kagan, C. R.; Donnio, B.; Murray, C. B. The Dendritic Effect and Magnetic Permeability in Dendron Coated Nickel and Manganese Zinc Ferrite Nanoparticles. *Nanoscale* **2017**, *9*, 13922−13928.

(4) Šutka, A.; Gross, K. A. Spinel Ferrite Oxide Semiconductor Gas Sensors. *Sens. Actuat. B: Chem.* **2016**, *222*, 95−105.

(5) Yang, H.; Bai, X.; Hao, P.; Tian, J.; Bo, Y.; Wang, X.; Liu, H. A Simple Gas Sensor Based on Zinc Ferrite Hollow Spheres: Highly Sensitivity, Excellent Selectivity and Long-Term Stability. *Sens. Actuat. B: Chem.* **2019**, *280*, 34−40.

(6) Hoque, S. M.; Hossain, M. S.; Choudhury, S.; Akhter, S.; Hyder, F. Synthesis and Characterization of Znfe2o4 Nanoparticles and Its Biomedical Applications. *Mater. Lett.* **2016**, *162*, 60−63.

(7) Somvanshi, S. B.; Kumar, R. V.; Kounsalye, J. S.; Saraf, T. S.; Jadhav, K. M. Investigations of Structural, Magnetic and Induction Heating Properties of Surface Functionalized Zinc Ferrite Nanoparticles for Hyperthermia Applications. *AIP Conf. Proc.* **2019**, *2115*, 030522.

(8) Bagade, A. A.; Ganbavle, V. V.; Mohite, S. V.; Dongale, T. D.; Sinha, B. B.; Rajpure, K. Y. Assessment of Structural, Morphological, Magnetic and Gas Sensing Properties of $CoFe_2O_4$ Thin Films. *J. Colloid Interface Sci.* **2017**, *497*, 181−192.

(9) Adak, N. C.; Chhetri, S.; Murmu, N. C.; Samanta, P.; Kuila, T. Analytical and Experimental Investigation on Magnetorheological Behavior of $CoFe_2O_4$-Rgo-Incorporated Epoxy Fluid Composites. *Adv. Comp. Hybrid Mater.* **2019**, *2*, 266−278.

(10) Ma, Y.; Lu, Y.; Gou, H.; Zhang, W.; Yan, S.; Xu, X. Octahedral $NiFe_2O_4$ for High-Performance Gas Sensor with Low Working Temperature. *Ceram. Int.* **2018**, *44*, 2620−2625.

(11) Vignesh, R. H.; Sankar, K. V.; Amaresh, S.; Lee, Y. S.; Selvan, R. K. Synthesis and Characterization of $MnFe_2O_4$ Nanoparticles for Impedometric Ammonia Gas Sensor. *Sens. Actuat. B: Chem.* **2015**, *220*, 50−58.

(12) Zhou, X.; Li, X.; Sun, H.; Sun, P.; Liang, X.; Liu, F.; Hu, X.; Lu, G. Nanosheet-Assembled $ZnFe_2O_4$ Hollow Microspheres for High-Sensitive Acetone Sensor. *ACS Appl. Materials & interfaces* **2015**, *7*, 15414−15421.

(13) Nikolic, M. V.; Vasiljevic, Z. Z.; Lukovic, M. D.; Pavlovic, V. P.; Krstic, J. B.; Vujancevic, J.; Tadic, N.; Vlahovic, B.; Pavlovic, V. B. Investigation of $ZnFe_2O_4$ Spinel Ferrite Nanocrystalline Screen-Printed Thick Films for Application in Humidity Sensing. *Int. J. Appl. Ceram. Technol.* **2019**, *16*, 981−993.

(14) Nemufulwi, M. I.; Swart, H. C.; Mdlalose, W. B.; Mhlongo, G. H. Size-Tunable Ferromagnetic $ZnFe_2O_4$ Nanoparticles and Their Ethanol Detection Capabilities. *Appl. Surf. Sci.* **2020**, *508*, 144863.

(15) Singh, H. H.; Sharma, H. B. Structural, Transport and Magnetic Properties of (1-X) $BiFeO_3$-$xCo_{0.7}Ni_{0.3}Fe_2O_4$ Nanocomposite Samples (X = 0.0, 0.2, 0.5, 0.8, 1.0). *Adv. Comp. Hybrid Mater.* **2020**, *3*, 609.

(16) Jimenez, V. O.; Kalappattil, V.; Eggers, T.; Bonilla, M.; Kolekar, S.; Huy, P. T.; Batzill, M.; Phan, M.-H. A Magnetic Sensor Using a 2d Van Der Waals Ferromagnetic Material. *Sci. Rep.* **2020**, *10*, 4789.

(17) Catto, A. C.; Silva, L. F. d.; Bernardi, M. I. B.; Bernardini, S.; Aguir, K.; Longo, E.; Mastelaro, V. R. Local Structure and Surface Properties of Co$_x$Zn$_{1-X}$O$_4$ Thin Films for Ozone Gas Sensing. *ACS Appl. Materials & interfaces* **2016**, *8*, 26066−26072.

(18) Pereira, P. F. S.; Gouveia, A. F.; Assis, M.; de Oliveira, R. C.; Pinatti, I. M.; Penha, M.; Gonçalves, R. F.; Gracia, L.; Andrés, J.; Longo, E. ZnWO4 Nanocrystals: Synthesis, Morphology, Photo-luminescence and Photocatalytic Properties. *Phys. Chem. Chem. Phys.* **2018**, *20*, 1923−1937.

(19) Angaiah, S.; Arunachalam, S.; Murugadoss, V.; Vijayakumar, G. A Facile Polyvinylpyrrolidone Assisted Solvothermal Synthesis of Zinc Oxide Nanowires and Nanoparticles and Their Influence on the Photovoltaic Performance of Dye Sensitized Solar Cell. *ES Energy Environ.* **2019**, *4*, 59−65.

(20) Waghmare, M.; Sonone, P.; Patil, P.; Kadam, V.; Pathan, H.; Ubale, A. Spray Pyrolytic Deposition of Zirconium Oxide Thin Films: Influence of Concentration on Structural and Optical Properties. *Eng. Sci.* **2018**, *5*, 79−87.

(21) Hou, C.-p.; Hou, J.; Zhang, H.; Ma, Y.; He, X.; Geng, W.; Zhang, Q. Facile Synthesis of LiMn$_{0.75}$Fe$_{0.25}$PO$_4$/C Nanocomposite Cathode Materials of Lithium-Ion Batteries through Microwave Sintering. *Eng. Sci.* **2020**, *11*, 36−43.

(22) Jayachandiran, J.; Arivanandhan, M.; Padmaraj, O.; Jayavel, R.; Nedumaran, D. Investigation on Ozone-Sensing Characteristics of Surface Sensitive Hybrid Rgo/WO$_3$ Nanocomposite Films at Ambient Temperature. *Adv. Comp. Hybrid Mater.* **2020**, *3*, 16−30.

(23) Gao, L.; Zhang, L.; Lyu, X.; Lu, G.; Liu, Q. Corrole Functionalized Iron Oxide Nanocomposites as Enhanced Peroxidase Mimic and Their Application in H$_2$O$_2$ and Glucose Colorimetric Sensing. *Eng. Sci.* **2018**, *1*, 69−77.

(24) Ben Ali, M.; El Maalam, K.; El Moussaoui, H.; Mounkachi, O.; Hamedoun, M.; Masrour, R.; Hlil, E. K.; Benyoussef, A. Effect of zinc concentration on the structural and magnetic properties of mixed Co-Zn ferrites nanoparticles synthesized by sol/gel method. *J. Magn. Magn. Mater.* **2016**, *398*, 20−25.

(25) Anchieta, C. G.; Severo, E. C.; Rigo, C.; Mazutti, M. A.; Kuhn, R. C.; Muller, E. I.; Flores, E. M. M.; Moreira, R. F. P. M.; Foletto, E. L. Rapid and Facile Preparation of Zinc Ferrite (ZnFe$_2$O$_4$) Oxide by Microwave-Solvothermal Technique and Its Catalytic Activity in Heterogeneous Photo-Fenton Reaction. *Mater. Chem. Phys.* **2015**, *160*, 141−147.

(26) Mady, A. H.; Baynosa, M. L.; Tuma, D.; Shim, J.-J. Facile Microwave-Assisted Green Synthesis of Ag- ZnFe$_2$O$_4$@Rgo Nano-composites for Efficient Removal of Organic Dyes under Uv- and Visible-Light Irradiation. *Appl. Catal. B Environ.* **2017**, *203*, 416−427.

(27) Meng, L.-Y.; Wang, B.; Ma, M.-G.; Lin, K.-L. The Progress of Microwave-Assisted Hydrothermal Method in the Synthesis of Functional Nanomaterials. *Mater. Today Chem.* **2016**, *1-2*, 63−83.

(28) Toby, B. H.; Von Dreele, R. B. Gsas-Ii: The Genesis of a Modern Open-Source All Purpose Crystallography Software Package. *J. Appl. Crystallogr.* **2013**, *46*, 544−549.

(29) Dovesi, R.; Erba, A.; Orlando, R.; Zicovich-Wilson, C. M.; Civalleri, B.; Maschio, L.; Rérat, M.; Casassa, S.; Baima, J.; Salustro, S.; Kirtman, B. Quantum-Mechanical Condensed Matter Simulations with Crystal. *Wiley Interdiscip. Rev.: Comput. Mol. Sci.* **2018**, *8*, No. e1360.

(30) Fritsch, D. Electronic and Optical Properties of Spinel Zinc Ferrite:Ab Initiohybrid Functional Calculations. *J. Phys.: Condens. Matter* **2018**, *30*, 095502.

(31) Monkhorst, H. J.; Pack, J. D. Special Points for Brillouin-Zone Integrations. *Phys. Rev. . B Condens. Matter Mater. Phys.* **1976**, *13*, 5188−5192.

(32) Rodríguez Torres, C. E.; Pasquevich, G. A.; Zélis, P. M.; Golmar, F.; Heluani, S. P.; Nayak, S. K.; Adeagbo, W. A.; Adeagbo, W. A.; Hergert, W.; Hoffmann, M.; Ernst, A.; Esquinazi, P.; Stewart, S. J. Oxygen-Vacancy-Induced Local Ferromagnetism as a Driving

Mechanism in Enhancing the Magnetic Response of Ferrites. *Phys. Rev. B* **2014**, *89*, 104411.

(33) Cheng, C. Long-Range Antiferromagnetic Interactions in ZnFe$_2$O$_4$ and CdFe$_2$O$_4$: Density Functional Theory Calculations. *Phys. Rev. B* **2008**, *78*, 132403.

(34) Guo, H.; Marschilok, A. C.; Takeuchi, K. J.; Takeuchi, E. S.; Liu, P. Essential Role of Spinel ZnFe$_2$O$_4$ Surfaces During Lithiation. *ACS Appl. Mater. Interfaces* **2018**, *10*, 35623−35630.

(35) Santiago, A. A. G.; Tranquilin, R. L.; Oliveira, M. C.; Ribeiro, R. A. P.; de Lazaro, S. R.; Correa, M. A.; Bohn, F.; Longo, E.; Motta, F. V.; Bomio, M. R. D. Disclosing the Structural, Electronic, Magnetic, and Morphological Properties of CuMnO$_2$: A Unified Experimental and Theoretical Approach. *J. Phys. Chem. C* **2020**, *124*, 5378.

(36) Ribeiro, R. A. P.; Andrés, J.; Longo, E.; Lazaro, S. R. Magnetism and Multiferroic Properties at MnTiO$_3$ Surfaces: A Dft Study. *Appl. Surf. Sci.* **2018**, *452*, 463−472.

(37) Ribeiro, R. A. P.; de Lazaro, S. R.; Gracia, L.; Longo, E.; Andrés, J. Theoretical Approach for Determining the Relation between the Morphology and Surface Magnetism of Co$_3$O$_4$. *J. Magn. Magn. Mater.* **2018**, *453*, 262−267.

(38) Ribeiro, R. A. P.; Lacerda, L. H. S.; Longo, E.; Andrés, J.; de Lazaro, S. R. Towards Enhancing the Magnetic Properties by Morphology Control of ATiO$_3$ (a = Mn, Fe, Ni) Multiferroic Materials. *J. Magn. Magn. Mater.* **2019**, *475*, 544−549.

(39) Avansi, W.; Catto, A. C.; da Silva, L. F.; Fiorido, T.; Bernardini, S.; Mastelaro, V. R.; Aguir, K.; Arenal, R. One-Dimensional V$_2$O$_5$/TiO$_2$ Heterostructures for Chemiresistive Ozone Sensors. *ACS Applied Nano Materials* **2019**, *2*, 4756−4764.

(40) Levy, D.; Pavese, A.; Hanfland, M. Phase Transition of Synthetic Zinc Ferrite Spinel (ZnFe$_2$O$_4$) at High Pressure, from Synchrotron X-Ray Powder Diffraction. *Phys. Chem. Miner.* **2000**, *27*, 638−644.

(41) Rao, K. J.; Vaidhyanathan, B.; Ganguli, M.; Ramakrishnan, P. A. Synthesis of Inorganic Solids Using Microwaves. *Chem. Mater.* **1999**, *11*, 882−895.

(42) Melo Quintero, J. J.; Rodríguez Torres, C. E.; Errico, L. A. Ab Initio Calculation of Structural, Electronic and Magnetic Properties and Hyperfine Parameters at the Fe Sites of Pristine ZnFe$_2$O$_4$. *J. Alloys Compd.* **2018**, *741*, 746−755.

(43) Chaudhari, P. R.; Gaikwad, V. M.; Acharya, S. A. Role of Mode of Heating on the Synthesis of Nanocrystalline Zinc Ferrite. *Applied Nanoscience* **2015**, *5*, 711−717.

(44) Singh, J. P.; Srivastava, R. C.; Agrawal, H. M.; Chand, P.; Kumar, R. Observation of Size Dependent Attributes on the Magnetic Resonance of Irradiated Zinc Ferrite Nanoparticles. *Current Applied Physics* **2011**, *11*, 532−537.

(45) Chandramohan, P.; Srinivasan, M. P.; Velmurugan, S.; Narasimhan, S. V. Cation Distribution and Particle Size Effect on Raman Spectrum of CoFe$_2$O$_4$. *J. Solid State Chem.* **2011**, *184*, 89−96.

(46) Howard, J. C.; Enyard, J. D.; Tschumper, G. S. Assessing the Accuracy of Some Popular Dft Methods for Computing Harmonic Vibrational Frequencies of Water Clusters. *J. Chem. Phys.* **2015**, *143*, 214103.

(47) Kubelka, P.; Munk, F. Ein Beitrag Zur Optik Der Farbanstriche. *Zeitschrift für Technische Physik* **1931**, *12*, 593.

(48) Wood, D. L.; Tauc, J. Weak Absorption Tails in Amorphous Semiconductors. *Phys. Rev. B* **1972**, *5*, 3144−3151.

(49) Andersen, H. L.; Saura-Múzquiz, M.; Granados-Miralles, C.; Canévet, E.; Lock, N.; Christensen, M. Crystalline and Magnetic Structure-Property Relationship in Spinel Ferrite Nanoparticles. *Nanoscale* **2018**, *10*, 14902−14914.

(50) Chu, X.; Jiang, D.; Zheng, C. The Gas-Sensing Properties of Thick Film Sensors Based on Nano- ZnFe$_2$O$_4$ Prepared by Hydrothermal Method. *Materials Science and Engineering: B* **2006**, *129*, 150−153.

(51) Pradeep, A.; Priyadharsini, P.; Chandrasekaran, G. Structural, Magnetic and Electrical Properties of Nanocrystalline Zinc Ferrite. *J. Alloys Compd.* **2011**, *509*, 3917−3923.

(52) Longo, V. M.; Cavalcante, L. S.; de Figueiredo, A. T.; Longo, E.; Varela, J. A.; Sambrano, J. R.; Paskocimas, C. A.; De Vicente, F. S.; Hernandes, A. C.; Hernandes, A. C. Highly Intense Violet-Blue Light Emission at Room Temperature in Structurally Disordered SrZrO$_3$ Powders. *Appl. Phys. Lett.* **2007**, *90*, 091906.

(53) Lin, J.; Ding, X.; Hong, C.; Pang, Y.; Chen, L.; Liu, Q.; Zhang, X.; Xin, H.; Wang, X. Several Biological Benefits of the Low Color Temperature Light-Emitting Diodes Based Normal Indoor Lighting Source. *Sci. Rep.* **2019**, *9*, 7560.

(54) Wulff, G. Xxv. Zur Frage Der Geschwindigkeit Des Wachsthums Und Der Auflösung Der Krystallflächen. *Zeitschrift für Kristallographie—Crystalline Materials* **1901**, *34*, 449.

(55) Lv, H.; Ma, L.; Zeng, P.; Ke, D.; Peng, T. Synthesis of Floriated ZnFe$_2$O$_4$ with Porous Nanorod Structures and Its Photocatalytic Hydrogen Production under Visible Light. *J. Mater. Chem.* **2010**, *20*, 3665−3672.

(56) Zhang, N.; Ruan, S.; Han, J.; Yin, Y.; Li, X.; Liu, C.; Adimi, S.; Wen, S.; Xu, Y. Oxygen Vacancies Dominated CuO@ ZnFe$_2$O$_4$ Yolk-Shell Microspheres for Robust and Selective Detection of Xylene. *Sens. Actuat. B: Chem.* **2019**, *295*, 117−126.

(57) Lv, L.; Wang, Y.; Cheng, P.; Zhang, B.; Dang, F.; Xu, L. Ultrasonic Spray Pyrolysis Synthesis of Three-Dimensional ZnFe$_2$O$_4$-Based Macroporous Spheres for Excellent Sensitive Acetone Gas Sensor. *Sens. Actuat. B: Chem.* **2019**, *297*, 126755.

(58) Pereira, P. F. S.; Gouveia, A. F.; Assis, M.; de Oliveira, R. C.; Pinatti, I. M.; Penha, M.; Gonçalves, R. F.; Gracia, L.; Andrés, J.; Longo, E. ZnWO$_4$ Nanocrystals: Synthesis, Morphology, Photo-luminescence and Photocatalytic Properties. *Phys. Chem. Chem. Phys.* **2018**, *20*, 1923−1937.

(59) Amoresi, R. A. C.; Oliveira, R. C.; Marana, N. L.; de Almeida, P. B.; Prata, P. S.; Zaghete, M. A.; Longo, E.; Sambrano, J. R.; Simões, A. Z. CeO$_2$ Nanoparticle Morphologies and Their Corresponding Crystalline Planes for the Photocatalytic Degradation of Organic Pollutants. *ACS Applied Nano Materials* **2019**, *2*, 6513−6526.

(60) Knobel, M.; Nunes, W. C.; Socolovsky, L. M.; De Biasi, E.; Vargas, J. M.; Denardin, J. C. Superparamagnetism and Other Magnetic Features in Granular Materials: A Review on Ideal and Real Systems. *J. Nanosci. Nanotechnol.* **2008**, *8*, 2836−2857.

(61) Carvalho, M. H.; Lima, R. J. S.; Meneses, C. T.; Folly, W. S. D.; Sarmento, V. H. V.; Coelho, A. A.; Duque, J. G. S. Determination of the Effective Anisotropy Constant of CoFe$_2$O$_4$ Nanoparticles through the T-Dependence of the Coercive Field. *J. Appl. Phys.* **2016**, *119*, 093909.

(62) Blanco-Gutierrez, V.; Saez-Puche, R.; Torralvo-Fernandez, M. J. Superparamagnetism and Interparticle Interactions in ZnFe$_2$O$_4$ Nanocrystals. *J. Mater. Chem.* **2012**, *22*, 2992−3003.

(63) Mendonça, E. C.; Jesus, C. B. R.; Folly, W. S. D.; Meneses, C. T.; Duque, J. G. S.; Coelho, A. A. Temperature Dependence of Coercive Field of ZnFe$_2$O$_4$ Nanoparticles. *J. Appl. Phys.* **2012**, *111*, 053917.

(64) Doan, L.; Lu, Y.; Karatela, M.; Phan, V.; Jeffryes, C.; Benson, T.; Wujcik, E. K. Surface Modifications of Superparamagnetic Iron Oxide Nanoparticles with Polylactic Acid-Polyethylene Glycol Diblock Copolymer and Graphene Oxide for a Protein Delivery Vehicle. *Eng. Sci.* **2019**, *7*, 10−16.

(65) An, Y.; Feng, S.; Shao, G.; Yuan, W.; Sun, K.; Li, X.; Fan, R. Influence of the Annealing Process on Magnetic Performance of Iron Based Soft Magnetic Composites. *Eng. Sci.* **2020**, *11*, 85−91.

(66) Wu, K.; Li, J.; Zhang, C. Zinc Ferrite Based Gas Sensors: A Review. *Ceram. Int.* **2019**, *45*, 11143−11157.

(67) Kim, H.-J.; Lee, J.-H. Highly Sensitive and Selective Gas Sensors Using P-Type Oxide Semiconductors: Overview. *Sens. Actuat. B: Chem.* **2014**, *192*, 607−627.

(68) Suematsu, K.; Watanabe, K.; Yuasa, M.; Kida, T.; Shimanoe, K. Effect of Ambient Oxygen Partial Pressure on the Hydrogen Response of SnO$_2$ Semiconductor Gas Sensors. *J. Electrochem. Soc.* **2019**, *166*, B618−B622.

(69) Ren, J.; Wang, Y.; Zhao, J.; Tan, S.; Petek, H. K Atom Promotion of O$_2$ Chemisorption on Au(111) Surface. *J. Am. Chem. Soc.* **2019**, *141*, 4438−4444.

(70) Cheng, X.; Jiang, X.; Tao, K.; Su, Q.; Wang, Y.; Xie, E. Microscopic Nature of Gas Adsorption on WO$_3$ Surfaces: Electron Interaction and Localization. *J. Phys. Chem. Lett.* **2020**, *11*, 9070−9078.